Author Manuscript

Author Manuscript

Author Manuscript

Author Manuscript

HHS Public Access

Author manuscript

*J Dent*. Author manuscript; available in PMC 2016 August 01.

Published in final edited form as:

*J Dent*. 2015 August ; 43(8): 1032–1042. doi:10.1016/j.jdent.2015.03.005.

# Assessment of remineralization via measurement of dehydration rates with thermal and near-IR reflectance imaging

**Robert C. Lee**, **Cynthia L. Darling**, and **Daniel Fried***

University of California, San Francisco, San Francisco, CA 94143-0758

## Abstract

**Objectives—**Previous studies have demonstrated that the optical changes due to the loss of water from porous lesions can be exploited to assess lesion severity with QLF, thermal and near-IR imaging. Since arrested lesions are less permeable to water due to the highly mineralized surface layer, changes in the rate of water loss can be related to changes in lesion structure. The purpose of this study was to investigate whether the rate of water loss correlates with the degree of remineralization and whether that rate can be measured using thermal and near-IR reflectance imaging.

**Methods—**Artificial bovine enamel lesions (n=30) were prepared by immersion in a demineralization solution for either 8 and 24 hours and they were subsequently placed in an acidic remineralization solution for different periods. The samples were dehydrated using an air spray for 30 seconds and surfaces were imaged using a thermal camera and an InGaAs camera at 1300–1700 nm wavelengths.

**Results—**The area enclosed by the time-temperature curve, Δ Q, from thermal imaging showed significant differences ($P<0.05$) between the lesion window and other windows. Near-IR reflectance intensity differences, Δ I, before and after dehydration decreased with longer periods of remineralization. Only near-IR reflectance imaging was capable of detecting significant differences ($P<0.05$) between the different periods of remineralization.

**Conclusions—**This study demonstrated that both thermal and near-IR reflectance imaging were suitable for the detection of remineralization in simulated caries lesions and near-IR wavelengths longer than 1400 nm are well suited for the assessment of remineralization.

### Keywords

dental caries; lesion activity; remineralization; near-IR imaging; thermal imaging; optical coherence tomography

*Corresponding Author: Daniel Fried, Professor, Department of Preventive and Restorative Dental Sciences, University of California, San Francisco, San Francisco, 707 Parnassus Ave. 94143, Phone: (415) 502-6641, Fax: (415) 502-6642, daniel.fried@ucsf.edu.

**Publisher's Disclaimer:** This is a PDF file of an unedited manuscript that has been accepted for publication. As a service to our customers we are providing this early version of the manuscript. The manuscript will undergo copyediting, typesetting, and review of the resulting proof before it is published in its final citable form. Please note that during the production process errors may be discovered which could affect the content, and all legal disclaimers that apply to the journal pertain.

Author Manuscript Author Manuscript Author Manuscript Author Manuscript

## 1. Introduction

Dental caries is a major oral health problem in most industrialized countries. (1) Since the introduction of fluoride to the drinking water, use of fluoride dentifrices and rinses, application of topical fluoride in dental office and improved dental hygiene, the rate of dental caries declined significantly. (2–4) Fluoride slows demineralization and enhances remineralization by promoting crystal growth and producing fluorapatite crystals that are much more resistant to acid challenge than the original hydroxyapatite of enamel and dentin. Lesions can be arrested by the preferential deposition of mineral at the lesion surface that inhibits diffusion. (5–7) An accurate assessment of lesion activity and severity is paramount for clinical diagnosis. Current methods for lesion assessment are composed of visual and tactile exams, which are prone to subjective bias, interference from staining, are limited to exposed surfaces and may cause permanent damage to the tooth structure. (3, 8) In addition, arrested lesions still retain the white coloration due to reflectance from the underlying body of the lesion (4), which may lead to an incorrect diagnosis of caries activity. (8) Gold standards for lesion assessment such as transverse microradiography (TMR) and polarized light microscopy (PLM) require destruction of the tooth, and are unsuitable for use *in-vivo*. New methods are needed to assess lesion activity and avoid unnecessary cavity preparations. Several studies have demonstrated that PS-OCT is uniquely capable of this task since it provides a measurement of the reflectivity from each layer of the lesion and is able to show the formation of a zone of increased mineral density and reduced light scattering due to remineralization. (9–11) In a previous PS-OCT study, we developed approaches to automatically detect the surface layer and measure its thickness with high accuracy. (12)

Early caries lesions can be described as non-cavitated subsurface lesions with an intact surface layer. (4) The lesion body manifests increased porosity due to mineral loss while the surface layer is maintained due to mineral deposition from the saliva. Mobile water filling the pores of the lesion body can evaporate through micropores in the surface layer. (13) As the lesion becomes arrested or undergoes remineralization, the permeability of the surface layer significantly decreases. (14) Thus, the rate of evaporation of water from the lesion depends on the lesion structure. The optical changes associated with water loss have been exploited via quantitative light-induced fluorescence (QLF) (15), thermal imaging (16, 17) and near-IR imaging. (18) Evaporation of water from a lesion is an endothermic process, which causes a temperature decrease followed by a recovery to thermal equilibrium as the lesion becomes dry. Kaneko et al. (16) and Zakian et al. (17) carried out thermal imaging studies using an infrared camera and an air-jet for evaporation on occlusal and smooth natural tooth surfaces. Ando et al. (19) reported that pulse thermography is sensitive to the mineralization state of the tooth and has potential to be used in lesion activity assessment.

Near-infrared (near-IR) imaging has been also exploited for caries detection since sound enamel is transparent in the near-IR and the scattering coefficient increases exponentially with increasing mineral loss. (20) Wu et al. (21) and Lee et al. (22) reported that reflectance and transillumination imaging were able to show demineralization on buccal and occlusal surfaces with high contrast at near-IR wavelengths. Zakian et al. (23) carried out near-IR reflectance measurements from 1000–2500 nm using a hyperspectral imaging system and showed that the reflectance from sound tooth areas decreases at longer wavelengths where

Author Manuscript Author Manuscript Author Manuscript Author Manuscript

water absorption is higher. Recent studies at near-IR wavelengths coincident with high water absorption, i.e. 1460 nm and > 1500-nm for artificial and natural lesions demonstrated extremely high lesion contrast. (24–26) In this study, near-IR reflectance imaging was used to determine if this phenomenon could be similarly exploited to monitor remineralization.

In a previous study, we found that the mean attenuation coefficient of enamel increased significantly at 1310 nm if samples are dehydrated. (24, 27) This suggests that changes in water content have a more profound effect on enamel transparency at near-IR wavelengths than in the visible. Usenik et al. (18) demonstrated that the rate of water evaporation from enamel increased with the severity of demineralization using near-IR hyperspectral imaging and that the water content could be estimated with an appropriate drying model. The magnitude of water absorption increases between 1400 and 1700 nm and we hypothesize these near-IR wavelengths are more sensitive to changes in lesion hydration. (24)

The influence of hydration on enamel lesions can be investigated as an indirect indicator of the decreased permeability of water due to remineralization. In this study, we measured optical changes in simulated enamel lesions that have undergone remineralization during controlled drying using thermography and near-IR reflectance imaging.

## 2. Material and methods

### 2.1. Sample preparation

Enamel blocks (n = 30), approximately 8–12 mm in length with a width of 2 mm and a thickness of 3 mm were prepared from extracted bovine incisors acquired from a slaughterhouse. The surfaces of the bovine enamel blocks were ground to a 9 μm finish. Each sample was partitioned into six regions or windows (1 sound control, 4 lesion and 1 remineralization control) by etching small incisions 1.8 mm apart across each of the enamel blocks using a laser. Incisions were etched using a transverse excited atmospheric pressure (TEA) $CO_2$ laser, an Impact 2500, GSI Lumonics (Rugby, UK), operating at 9.3 μm with a pulse duration of 15 μs, a pulse repetition rate of 200 Hz and a fluence of 20 J/cm$^2$.

A thin layer of acid-resistant varnish in the form of nail polish, Revlon (New York, NY), was applied to protect the sound and remineralization control windows before exposure to the demineralization solution. Two groups (n = 15 per group) of enamel samples each with four exposed lesion windows were immersed in 45 mL aliquots of the demineralization solution for 8 and 24 hours, respectively. The demineralization solution, which was maintained at 37°C and pH 4.8, was composed of 2.0 mmol/L calcium, 2.0 mmol/L phosphate and 0.075 mol/L acetate. After the demineralization period, the acid resistant varnish was removed by immersion in acetone in an ultrasonic bath for 15 minutes and the acid-resistant varnish was applied again to the sound and lesion windows.

Sample windows were subsequently exposed to an acidic remineralization solution for 4, 8 or 12-days by covering appropriate windows with acid resistant varnish at each time point. It has been hypothesized that the lower pH reduces preferential deposition of mineral in the lesion surface, enhancing remineralization of the lesion body. (28) The acidic remineralization solution was composed of 4.1 mmol/L calcium, 15 mmol/L phosphate, 50

Author Manuscript Author Manuscript Author Manuscript Author Manuscript

mmol/L lactic acid, 20 mmol/L HEPES buffer and 2 ppm $F^-$ maintained at 37°C and a pH of 4.8. (28) The remineralization control window was exposed to the acidic remineralization solution for 12 days in order to examine its effect on sound enamel. After the 12 days of remineralization, the acid resistant varnish was removed and the samples were stored in 0.1 % thymol solution to prevent fungal and bacterial growth.

### 2.2. PS-OCT system

The PS-OCT system used in this study has been described previously. (29) An all fiber-based Optical Coherence Domain Reflectometry (OCDR) system with polarization maintaining (PM) optical fiber, high speed piezoelectric fiber-stretchers and two balanced InGaAs receivers that was designed and fabricated by Optiphase, Inc., Van Nuys, CA was used to acquire the images. (30) This two-channel system was integrated with a broadband superluminescent diode (SLD) DL-CS3159A, Denselight (Jessup, MD) and a high-speed XY-scanning motion controller system, ESP 300 controller with ILS100PP and 850G-HS stages, (Newport, Irvine, CA) for *in-vitro* optical tomography. A high power (15 mW) polarized SLD source operated at a center wavelength of 1317 nm with a spectral bandwidth full-width-half-maximum (FWHM) of 84 nm was used to provide an axial resolution of 9 μm in air and 6 μm in enamel (refractive index = 1.6). Light from the sample arm was focused onto the sample surface using a 20 mm focal length plano-convex lens providing a lateral resolution of approximately 20 μm.

The PS-OCT system was completely controlled using LabView™ software (National Instruments, Austin, TX). Samples were dried with pressurized air for 30 seconds prior to scanning. Each B-scan consisted of 300 A-scans spaced 50 μm apart. The A-scan sweep rate was 150 Hz with a dynamic range of 48 dB and each A-scan was an average of 10 scans. The total number of data points in each A-scan was 2000 over a scan range of approximately 5 mm in air.

### 2.3. Calculation of transparent surface layer thickness, lesion depth and integrated reflectivity (ΔR)

PS-OCT images were processed using a dedicated program constructed with LabView™ software. There was a phase shift in the PM-fiber between the two axes, so an axial position calibration was performed once prior to the study. A gold mirror was scanned at a 150 Hz sweep rate and each A-scan was an average of 100 scans. Five hundred A-scans were acquired at 10 μm intervals over the entire scan range to determine the required axial position adjustments and the axial position of the cross-polarization scan images was adjusted to match the co-polarization scan images.

Image processing methods for surface layer detection and measurement method utilized an edge detection technique using the zero-crossing first-order derivative as described previously. (12, 31) In this study, the threshold values for the ratio of the intensities of the two peaks were further specified to 0.1 for the co-polarization axis and 0.5 for the cross-polarization axis.

Author Manuscript Author Manuscript Author Manuscript Author Manuscript

Previous studies have shown that the integrated reflectivity, ΔR, over the estimated lesion depth positively correlates with the integrated mineral loss (volume percent mineral loss × μm), ΔZ. (32, 33) ΔR was calculated by integrating from the base of the transparent layer through the entire estimated lesion body in the CP-OCT images. (12) This had the added advantage of removing the contribution of the high specular reflection at the surface of the transparent layer, which was large enough to be present even in the CP-OCT images.

A region of interest (ROI) was specified for the sound region from each sample in order to discriminate between demineralized and sound enamel. ΔR was calculated from the selected ROI and it was compared to the ΔR of the lesions in order to reduce false-positives in lesion detection. The transparent surface layer, lesion depth and ΔR measurements were estimated by averaging 25 A-scans from a 5 × 5 pixel region of interest. A 5 × 5 pixel median filter was applied to the final 2D projection images for improved visualization.

### 2.4. Dehydration measurements

The following setup was used for the dehydration experiments of sec. 2.5 and 2.6. Each sample was placed in a mount connected to a high-speed XY-scanning motion controller system, Newport ESP 300 controller & 850G-HS stages coupled with an air nozzle and a light source as shown in Fig. 1. All surfaces excluding the windows were covered with black nail polish, OPI (North Hollywood, CA) in order to confine water loss to the exposed surface and prevent the transmission of light through the sides of the sample. Each sample was immersed in the water bath for 30 seconds while being vigorously shaken to enhance water diffusion. After the sample was removed from the water bath, an image was captured as an initial reference image and the air spray was activated. The air pressure was set to 15 psi and the computer controlled air nozzle was positioned 2 cm away from the sample. Each measurement consisted of capturing a sequence of images at 4 frames per second for 30 seconds. For each measurement, the air nozzle and the light source were centered on the ROI, and this process was repeated for each window (6 times per sample). The dehydration setup was completely automated using LabView™ software. All windows from all samples were exposed to the same dehydration protocol.

### 2.5 Thermal imaging and analysis

A Model A65 infrared (IR) thermography camera (FLIR Systems, Wilsonville, OR) sensitive from 7.5 – 13 μm with a resolution of 640 × 512 pixels, a thermal sensitivity of 50 mK and a lens with a 13 mm focal length was used to record temperature changes during the dehydration process. The area per pixel was approximately 0.02 $mm^2$. The ambient temperature, flowing air temperature and water bath temperature were approximately 21 °C (294.15 K) and were consistent throughout the experiment. The object emissivity was set to 0.91 (34) and the atmospheric temperature was set to 294.15 K. Relative humidity was set at a default value of 50%; humidity values were not recorded, but every sample was measured under the same conditions. Previous studies have shown that ΔQ, the area enclosed by the time-temperature curve, can be used as a quantitative measure of porosity and can be used to discriminate between sound and demineralized enamel *in-vitro*. (16, 17)

Author Manuscript Author Manuscript Author Manuscript Author Manuscript

Thermal images were processed and analyzed using a dedicated program written in Labview™. The thermography camera outputs a series of temperature measurements over time. The initial reference temperature measurements varied slightly (± 0.5 K) due to the different emissivity, lesion structure, mineral composition and water content among windows. Calibration was carried out via matching the measurements from the initial reference image to the ambient temperature. ΔQ was calculated from the area enclosed by the initial temperature and the time-temperature curve, acquired from an average measurement of a 3 × 3 pixel, ROI for each window.

### 2.6 Near-IR reflectance imaging and analysis

An Indigo Alpha near-IR camera (FLIR Systems, Wilsonville, OR) with an InGaAs focal plane array, a spectral sensitivity range from 900 nm to 1750 nm, a resolution of 320 × 256 pixels and an InfiniMite™ lens (Infinity, Boulder, CO) was used to acquire all the images during the dehydration process. The area per pixel was approximately 0.003 $mm^2$. Light from a 150 W fiber-optic illuminator FOI-1 (E Licht Company, Denver, CO) was directed at the sample at an incident angle of approximately 60 ° in order to reduce specular reflection as shown in Fig. 1. Several band-pass (BP) and long-pass (LP) filters were used to provide different spectral distributions of near-IR light. Band-pass filters centered at 1300 nm with 90 nm bandwidth (1260–1340 nm), 1460 nm with 85 nm bandwidth (1420–1500 nm) (Spectrogon, Parsippany, NJ) and long-pass filters at 1400 nm (1400–1700 nm) and 1500 nm (1500–1700 nm) (FEL LP series from Thorlabs, Newton, NJ) were used. The illuminating light intensity was set to its maximum for 1300 nm BP, 1460 nm BP and 1500 nm LP filters and to 80% of the maximum for 1400 nm LP filter in order to avoid oversaturation. Source to sample distance was fixed at 5 cm for all samples.

Near-IR reflectance images were processed and automatically analyzed using a dedicated program constructed with LabView™ software. A 5 × 5 pixel ROI was specified for each window and an average measurement was recorded for each time point. The image contrast was calculated using $(I_L - I_S)/I_L$ for the final image (t = 30), where $I_S$ is the mean intensity of the sound enamel and $I_L$ is the mean intensity of the lesion. In addition to lesion contrast, the intensity difference between the final and initial images, ΔI(t=30), was calculated using $I(t=30) - I_I$, where I(t=30) is the mean intensity at t = 30 seconds and $I_I$ is the mean intensity prior to turning on the air nozzle.

In order to investigate the rate of intensity change in conjunction with the overall intensity change, the “S”-shaped time-intensity curve was fit to a sigmoid function:

$$I(t)=\frac{a}{1+e^{b(c-t)}}+d, \quad (1)$$

where I(t) is intensity value at time (t) in seconds and d was fixed at $I_I$. $I_I$ was substituted with d in Equation 1 to yield:

$$\Delta I(t)=\frac{a}{1+e^{b(c-t)}}. \quad (2)$$

Author Manuscript Author Manuscript Author Manuscript Author Manuscript

Some lesion windows exhibited a “bump” in the intensity profile as shown in Fig. 6A by the asterisk. If such phenomenon was observed, the time-intensity difference curve was cropped to ignore the excursion. This phenomenon was detected if an intensity value exceeded all measurements collected in the subsequent five seconds with at least a 2% difference. The Levenberg-Marquardt algorithm was used to estimate the best fit to equation 2 with parameters (*a*), (*b*) and (*c*). Since (*a*) represents the amplitude or the difference between two asymptotes of the sigmoid function and (*b*) represents the growth rate of the function, the product of these two parameters representing the overall growth rate (OGR) was calculated.

### 2.7 Polarized Light Microscopy (PLM) and Transverse Microradiography (TMR)

After sample imaging was completed, 200 μm thick serial sections were cut using an Isomet 5000 saw (Buehler, IL), for polarized light microscopy (PLM) and transverse microradiography (TMR). PLM was carried out using a Meiji Techno Model RZT microscope (Meiji Techno Co., LTD, Saitama, Japan) with an integrated digital camera, Canon EOS Digital Rebel XT (Canon Inc., Tokyo, Japan). The sample sections were imbibed in water and examined in the brightfield mode with crossed polarizers and a red I plate with 500 nm retardation. PLM images were acquired at 40x magnification and had a resolution of 3264 × 2448 pixels.

A custom built digital microradiography (TMR) system was used to measure the volume percent mineral content in the areas of demineralization on the tooth sections. (35) High-resolution microradiographs were taken using Cu Kα radiation from a Philips 3100 X-ray generator and a Photonics Science FDI X-ray digital imager, Microphotonics (Allentown, PA). The X-ray digital imager consisted of a 1392×1040 pixel interline CCD directly bonded to a coherent micro fiber-optic coupler that transfers the light from an optimized gadolinium oxysulfide scintillator to the CCD sensor. The pixel resolution was 2.1 μm and the images were acquired at 10 frames per second. A high-speed motion control system with Newport UTM150 and 850G stages and an ESP 300 controller coupled to a video microscopy and a laser targeting system was used for precise positioning of the sample in the field of view of the imaging system.

### 2.8 Statistical analysis

Sample groups were compared using repeated measures analysis of variance (ANOVA) with a Tukey–Kramer post hoc multiple comparison test. Linear regression with Pearson’s correlation was used to examine the relationship between data acquired from PS-OCT, PLM and TMR measurements. All statistical analyses were performed with 95% confidence with Prism™ (GraphPad software, San Diego, CA).

## 3. Results

Figure 2 shows the visible, PS-OCT and PLM images of one of the samples from the initial 24-hour demineralization group after exposure to remineralization. Windows exposed to the initial demineralization solution could be discriminated from sound and remineralization control windows by visual examination as shown in Fig. 2A, but not from the 4, 8, or 12-day remineralization windows. In contrast, the changes to the mineral subsurface structure upon

Author Manuscript Author Manuscript Author Manuscript Author Manuscript

demineralization and remineralization could be easily seen with PS-OCT and histology (PLM), Figs. 2D and 2E. The transparent surface layer was clearly visible in the PLM image of a cross-section (Fig. 2D) and the algorithm was able to detect the transparent surface layer highlighted in yellow in the CP-OCT b-scan image as shown in Fig. 2E. Even though the pH of the remineralization solution was acidic at 4.8, the remineralization control window was not affected by the supersaturated acidic calcifying solution with 2 ppm fluoride as shown in the PLM image (Fig. 2D) and no significant changes from the sound window were detected by PS-OCT (Figs. 2B, 2C and 2E). There was a significant increase in the thickness of transparent surface layer and a significant decrease in the lesion severity with increasing period of remineralization. The transparent surface layer thickness, lesion depth and lesion severity measurements taken with PS-OCT, PLM and TMR are listed in Table 1.

In our previous study, the algorithm successfully detected the transparent surface layers with high sensitivity (0.92) and high specificity (0.97). (12) In this study, the modified algorithm was able to detect the transparent surface layer without any false positives and false negatives. The total number of windows was 150 from 30 samples, with 90 true positives and 60 true negatives. The thickness of the transparent surface layer estimated with PS-OCT, showed a strong correlation with PLM measurements (Pearson's correlation, $p < 0.0001$, $R^2 = 0.61$). The correlation coefficient, $R^2$, reported in this study was weaker than the previously reported value ($R^2 = 0.90$ - ref (12)), likely due to the variations in the surface layer thickness (33 μm vs. 55 μm).

The time-lapse thermal images of the sample from Fig. 2 are shown in Fig. 3 and its time-temperature profiles are shown in Fig. 4A. With forced air-drying, most samples approached ambient temperature within 30 seconds. Figures 3 and 4A show that the lesion window exhibited the greatest temperature drop in the first 5 seconds of forced drying and manifested the slowest recovery to equilibrium. As the lesion was exposed to the remineralization solution, these changes became less noticeable and ΔQ measurements showed no significant difference from those of sound and the remineralization control windows as shown in Fig. 4B. The mean ΔQ of the lesion windows was significantly larger than those of all the other windows for both the 8-hour and 24-hour groups as shown in Table 2. Variations in magnitude of ΔQ for the samples of the initial 24-hour demineralization group were larger than those of the initial 8-hour demineralization group.

Time-lapse near-IR reflectance images acquired with the 1460 nm band-pass filter of the sample from Fig. 2 are shown in Fig. 5 and its time-intensity difference profile is shown in Fig. 6A. The intensity difference, ΔI(t), was recorded instead of raw intensity data due to differences in anatomical structure of the sample, i.e. variation in depth to DEJ, presence of cracks, enamel tufts and birefringence due to orientation of enamel spindles. Variation of ΔI(t=30) nicely followed changes in the lesion structure as shown in Fig. 6C and Table 3. As seen in Fig. 6A, the time-intensity difference profiles closely resembled a sigmoid function curve. In addition, 10 of the 15 lesion windows from the initial 24-hour demineralization group and one of the 15 lesion windows from initial 8-hour deminerlization group exhibited a sharp excursion in the intensity profiles. In the cases where the "bump", noted as * in Fig. 6A, was observed, curve fitting was performed ignoring that excursion for calculation of

Author Manuscript Author Manuscript Author Manuscript Author Manuscript

OGR. This phenomenon was confined only to the lesion windows with the most severe lesions. We explored this phenomenon further by imaging with crossed polarizers, which reduced specular reflection and successfully eliminated the bump from the profile. Therefore, it is likely that the excursion in the intensity profile is due to specular reflection from the surface of the lesion. Although the light source was directed at the sample at an incident angle of approximately 60°, the highly roughened and porous surface of the demineralized enamel may have deflected some specular reflection to the camera.

Near-IR reflectance performance was also analyzed at different wavelengths using four different filters as shown in Table 3. The 1300 nm band-pass (1260–1340 nm) filter yielded the lowest lesion contrast as well as the smallest differences among windows due to lower water absorption. The three other filters, 1460 nm band-pass (1420–1500 nm), 1400 nm long-pass (1400–1700 nm) and 1500 nm long-pass (1500–1700 nm), showed higher contrast.

There was considerable variation in contrast from sample to sample (large standard deviation) due to structural variations and in a few cases negative contrast values were measured. The use of intensity difference values provided more consistent results; $\Delta I(t=30)$ manifested a decrease in intensity with increasing degree of remineralization with a 3 – 4 fold difference in magnitude between the sound and lesion windows for the samples treated for both the initial 8-hour and 12-hour demineralization groups, Fig. 6C. OGR also showed a decreasing trend as the lesion remineralized displaying greater differences between the sound and lesion windows compared to the intensity difference (Fig. 6D); the sound and lesion windows of the samples treated with the initial 24-hour demineralization showed an approximately 20 fold difference and those treated with the initial 8-hour demineralization showed an approximately 4 fold difference. Most importantly, OGR showed a significant difference between the lesion and the 4-day remineralization window while that difference was not significant for $\Delta I(t=30)$.

## 4. Discussion

This study suggests that both the thermal and near-IR reflectance imaging modalities are suitable for monitoring enamel remineralization. Enamel is permeable (36) and it is composed of approximately 96 % mineral and up to 3% water by weight. (37) Demineralized enamel can lose as much as 41% of its mineral content near the surface of the lesion by acid dissolution and remain intact as shown by depth-mineral density profiles from TMR (38) and these pores are occupied by mobile water after demineralization. (13, 39) However, in remineralized lesions, the highly mineralized surface layer inhibits free diffusion from the lesion body to the outer surface. Therefore, the rate of loss of mobile water from the lesion is likely to be highly dependent on the thickness and mineral content of that highly mineralized surface layer.

During the dehydration process, heat loss is caused by two major mechanisms: the varying temperature between the flowing air and the sample, as well as the highly endothermic evaporation of water molecules from the surface of the sample. (13) Kaneko et al. (16) reported that thermography data could be used to obtain quantitative information on the

Author Manuscript Author Manuscript Author Manuscript Author Manuscript

extent of demineralization such as lesion area, mineral loss and lesion depth and that ΔQ was correlated with ΔZ. Zakian et al. (17) showed that ΔQ maps created on the tooth occlusal surface manifested high correlation with histological scores based on visual diagnosis.

We expected ΔQ to decrease as the lesion was exposed to the remineralization solution. Although there were significant differences in the mean ΔQ values between the lesion and the other windows, thermal imaging failed to show significant differences between the individual remineralization windows or between the sound and remineralization windows as shown in Fig. 4 and Table 2.

Changes in water and mineral composition due to demineralization can be observed as changes in optical properties such as light scattering and birefringence. (40, 41) Since sound enamel is virtually transparent in the near-IR with optical attenuation 1–2 orders magnitude less than in the visible, demineralized enamel can be discriminated from sound enamel with high contrast at near-IR wavelengths. (24–26) In a previous study, it was shown that the state of hydration of the tooth had a profound effect on the optical transparency of sound enamel; empty pores act as scattering sites at near-IR wavelengths. (24) Figure 6 and Table 3 show a decreasing trend in lesion contrast measurements with periods of remineralization at all near-IR wavelengths. Wavelengths between 1400 nm and 1700 nm yielded the largest differences between windows due to increased absorption by water. (24) However, the lesion contrast measurements were highly variable due to anatomical variation among samples and ΔI(t) was employed to minimize this discrepancy. The ΔI(t) profiles closely resembled a sigmoid function and OGR was calculated from the curve-fit to explain their behavior. Figure 6D and Table 3 show that OGR is also useful for detecting and assessing progression of remineralization.

## 5. Conclusions

In summary, the highly mineralized surface layer plays an important role in the dehydration process of remineralized enamel lesions. It appears that both the thermal and near-IR imaging methods are suitable for detection of remineralization and are therefore highly promising for the clinical assessment of lesion activity. However, near-IR reflectance imaging at wavelengths between 1400 nm and 1700 nm was also capable of detecting significant differences between different periods of remineralization and was therefore the most effective for imaging during the dehydration process.

## References

1. Petersen PE. The World Oral Health Report 2003: continuous improvement of oral health in the 21st century--the approach of the WHO Global Oral Health Programme. Community Dentistry and Oral Epidemiology. 2003; 31 (Suppl 1):3–23. [PubMed: 15015736]
2. Fluorides and oral health. . Report of a WHO Expert Committee on Oral Health Status and Fluoride Use. World Health Organization technical report series. 1994; 846:1–37. [PubMed: 7975675]
3. NIH. Diagnosis and Management of Dental Caries throughout Life. NIH Consensus Statement. 2001; 18(1):1–24. [PubMed: 11699634]
4. Fejerskov, O.; Kidd, E., editors. Dental Caries: The Disease and its Clinical Management. Oxford: Blackwell; 2003.

Author Manuscript Author Manuscript Author Manuscript Author Manuscript


5. ten Cate JM, Featherstone JDB. Mechanistic aspects of the interactions between fluoride and dental enamel. Critical Reviews in Oral Biology & Medicine. 1991; 2:283–96. [PubMed: 1892991]
6. ten Cate JM, Arends J. Remineralization of artificial enamel lesions in vitro. Caries Research. 1977; 11(5):277–86. [PubMed: 18285]
7. Kidd EA. The histopathology of enamel caries in young and old permanent teeth. British Dental Journal. 1983; 155(6):196–8. [PubMed: 6578821]
8. Ekstrand KR, Zero DT, Martignon S, Pitts NB. Lesion activity assessment. Monographs in Oral Science. 2009; 21:63–90. [PubMed: 19494676]
9. Manesh SK, Darling CL, Fried D. Polarization-sensitive optical coherence tomography for the nondestructive assessment of the remineralization of dentin. Journal of Biomedical Optics. 2009; 14(4):044002. [PubMed: 19725714]
10. Kang H, Jiao JJ, Lee C, Le MH, Darling CL, Fried D. Nondestructive Assessment of Early Tooth Demineralization Using Cross-Polarization Optical Coherence Tomography. IEEE journal of selected topics in quantum electronics. 2010; 16(4):870–76. [PubMed: 21660217]
11. Jones RS, Darling CL, Featherstone JD, Fried D. Remineralization of in vitro dental caries assessed with polarization-sensitive optical coherence tomography. Journal of Biomedical Optics. 2006; 11(1):014016. [PubMed: 16526893]
12. Lee RC, Kang H, Darling CL, Fried D. Automated assessment of the remineralization of artificial enamel lesions with polarization-sensitive optical coherence tomography. Biomedical Optics Express. 2014; 5(9):2950–62. [PubMed: 25401009]
13. Zahradnik RT, Moreno EC. Progressive stages of subsurface demineralization of human tooth enamel. Archieves of Oral Biology. 1977; 22(10–11):585–91.
14. Lepri TP, Colucci V, Turssi CP, Corona SA. Permeability of eroded enamel following application of different fluoride gels and $CO_2$ laser. Lasers in Medical Science. 2013; 28(1):235–40. [PubMed: 22639231]
15. Ando M, Stookey GK, Zero DT. Ability of quantitative light-induced fluorescence (QLF) to assess the activity of white spot lesions during dehydration. American Journal of Dentistry. 2006; 19(1): 15–8. [PubMed: 16555651]
16. Kaneko, K.; Matsuyama, K.; Nakashima, S. Early detection of Dental caries II. Indiana University; 1999. Quantification of Early Carious Enamel Lesions by using an Infrared Camera; p. 83-99.
17. Zakian CM, Taylor AM, Ellwood RP, Pretty IA. Occlusal caries detection by using thermal imaging. Journal of Dentistry. 2010; 38(10):788–95. [PubMed: 20599464]
18. Usenik P, Bürmen M, Fidler A, Pernuš F, Likar B. Near-infrared hyperspectral imaging of water evaporation dynamics for early detection of incipient caries. Journal of Dentistry. 2014; 42(10): 1242–7. [PubMed: 25150104]
19. Ando M, Sharp N, Adams D. Pulse thermography for quantitative nondestructive evaluation of sound, de-mineralized and re-mineralized enamel. Proceedings of SPIE: Medical and Biological Applications I. 2012; 83480S:1–7.
20. Darling CL, Huynh GD, Fried D. Light scattering properties of natural and artificially demineralized dental enamel at 1310 nm. Journal of Biomedical Optics. 2006; 11(3):34023. [PubMed: 16822072]
21. Wu J, Fried D. High contrast near-infrared polarized reflectance images of demineralization on tooth buccal and occlusal surfaces at lambda = 1310-nm. Lasers in Surgery and Medicine. 2009; 41(3):208–13. [PubMed: 19291753]
22. Lee D, Fried D, Darling C. Near-IR multi-modal imaging of natural occlusal lesions. Proceedings of SPIE: Lasers in Dentistry XV. 2009; 71620X:1–7.
23. Zakian C, Pretty I, Ellwood R. Near-infrared hyperspectral imaging of teeth for dental caries detection. Journal of Biomedical Optics. 2009; 14(6):064047. [PubMed: 20059285]
24. Chung S, Fried D, Staninec M, Darling CL. Multispectral near-IR reflectance and transillumination imaging of teeth. Biomedical Optics Express. 2011; 2(10):2804–14. [PubMed: 22025986]
25. Fried WA, Darling CL, Chan K, Fried D. High Contrast Reflectance Imaging of Simulated Lesions on Tooth Occlusal Surfaces at Near-IR Wavelengths. Lasers in Surgery and Medicine. 2013; 45:533–41. [PubMed: 23857066]

Author Manuscript Author Manuscript Author Manuscript Author Manuscript


26. Simon JC, Chan KH, Darling CL, Fried D. Multispectral near-IR reflectance imaging of simulated early occlusal lesions: Variation of lesion contrast with lesion depth and severity. Lasers in Surgery and Medicine. 2014; 46(3):203–15. [PubMed: 24375543]
27. Maung LH, Lee C, Fried D. Near-IR Imaging of thermal changes in enamel during laser ablation. Proceedings of SPIE: Lasers in Dentistry XVI. 2010; 754902:1–6.
28. Yamazaki H, Margolis HC. Enhanced enamel remineralization under acidic conditions in vitro. Journal of Dental Research. 2008; 87(6):569–74. [PubMed: 18502967]
29. Fried D, Xie J, Shafi S, Featherstone JDB, Breunig T, Lee CQ. Early detection of dental caries and lesion progression with polarization sensitive optical coherence tomography. Journal of Biomedical Optics. 2002; 7(4):618–27. [PubMed: 12421130]
30. Bush J, Davis P, Marcus MA. All-Fiber Optic Coherence Domain Interferometric Techniques. Proceedings of SPIE: Fiber Optic Sensor Technology II. 2000; 4204:71–80.
31. Lee RC, Darling CL, Fried D. Automated detection of remineralization in simulated enamel lesions with PS-OCT. Proceedings of SPIE: Lasers in Dentistry XX. 2014; 89290E:1–8.
32. Jones RS, Darling CL, Featherstone JD, Fried D. Imaging artificial caries on the occlusal surfaces with polarization-sensitive optical coherence tomography. Caries Research. 2006; 40(2):81–89. [PubMed: 16508263]
33. Ngaotheppitak P, Darling CL, Fried D. Polarization Optical Coherence Tomography for the Measuring the Severity of Caries Lesions. Lasers in Surgery and Medicine. 2005; 37(1):78–88. [PubMed: 15889402]
34. Lin M, Liu QD, Xu F, Bai BF, Lu TJ. In vitro investigation of heat transfer in human tooth. Proceedings of SPIE: Experimental Mechanics IV. 2009; 75222N:1–7.
35. Darling CL, Featherstone JDB, Le CQ, Fried D. An automated digital microradiography system for assessing tooth demineralization. Proceedings of SPIE: Lasers in Dentistry VX. 2009; 71620T:1–7.
36. Atkinson HF. An investigation into the permeability of human enamel using osmotic methods. British Dental Journal. 1947; 83(10):205–14. [PubMed: 18918880]
37. Weatherell JA. Composition of dental enamel. British Medical Bulletin. 1975; 31(2):115–9. [PubMed: 1164600]
38. Arends J, Ruben JL, Inaba D. Major topics in quantitative microradiography of enamel and dentin: R parameter, mineral distribution visualization, and hyper-remineralization. Advances in Dental Research. 1997; 11(4):403–14. [PubMed: 9470497]
39. Myers HM. Trapped water of dental enamel. Nature. 1965; 206(985):713–4. [PubMed: 5832855]
40. Baumgartner A, Dicht S, Hitzenberger CK, Sattmann H, Robi B, Moritz A, Fercher AF, Sperr W. Polarization-sensitive optical optical coherence tomography of dental structures. Caries Research. 2000; 34:59–69. [PubMed: 10601786]
41. Zhang XZ, Anderson P, Dowker SE, Elliott JC. Optical profilometric study of changes in surface roughness of enamel during in vitro demineralization. Caries Research. 2000; 34(2):164–74. [PubMed: 10773635]

Author Manuscript Author Manuscript Author Manuscript Author Manuscript

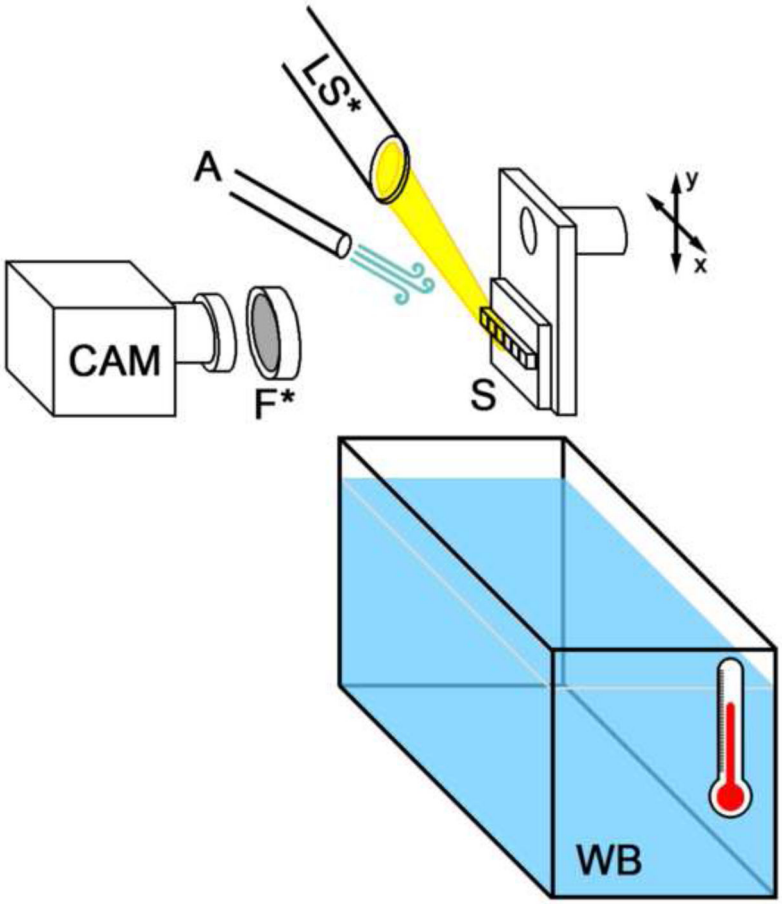


**Fig. 1.**

Dehydration experimental setup: CAM: image capturing device, A: compressed air nozzle, LS*: tungsten light source, S: sample, F*: filter, WB: water bath

*Light source and filter were absent in the thermal imaging setup.

Author Manuscript Author Manuscript Author Manuscript Author Manuscript

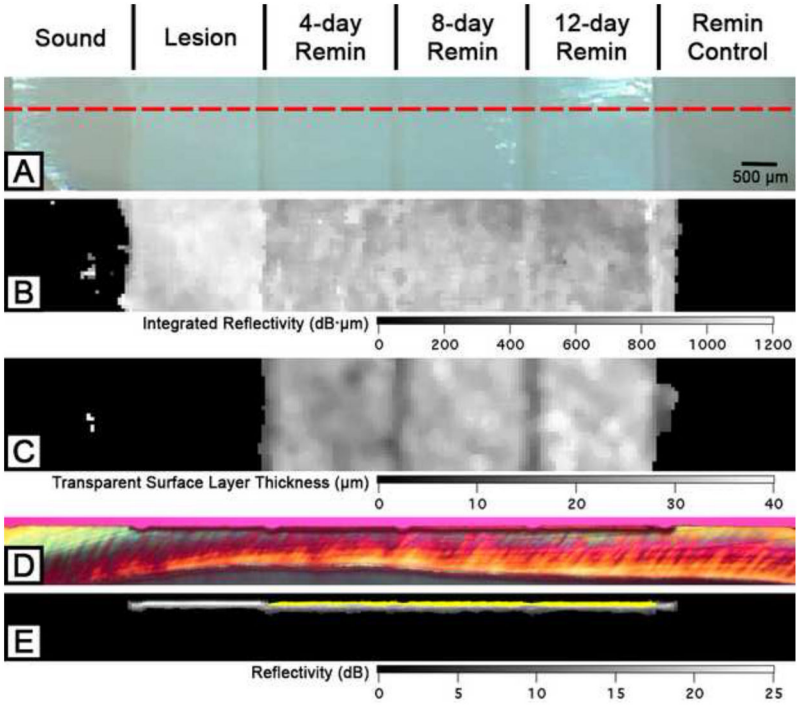


**Fig. 2.**

Two-dimensional projection and cross-sectional PLM and OCT images of the six windows on a 24-hour demineralization sample. The red dotted line in the visible light reflectance image (A) represents the position of the section shown in (D) and (E). Two-dimensional OCT surface projection images of the same sample are shown including (B) integrated reflectivity and (C) the transparent surface layer thickness. PLM (D) and processed CP-OCT B-scan (E) images show an increase in transparent surface layer thickness over the periods of exposure to the remineralizing solution. The transparent surface layer is highlighted in yellow (E).

Author Manuscript Author Manuscript Author Manuscript Author Manuscript

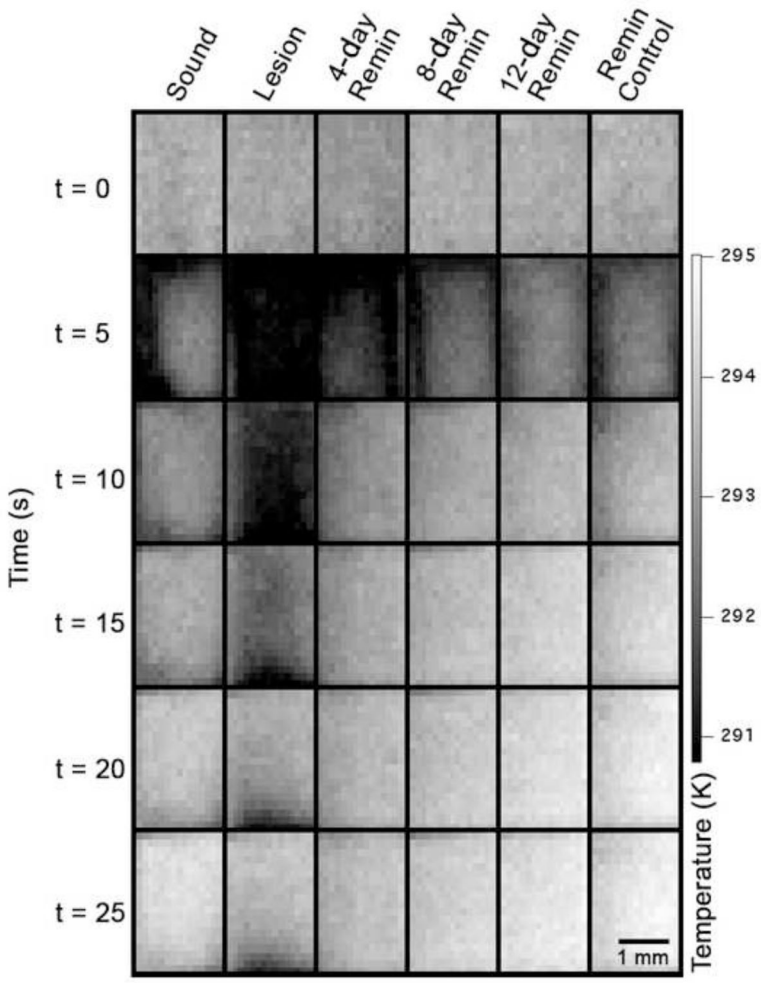


**Fig. 3.**

Time-lapse thermal images of the sample shown in Fig. 2. Time axis on left represents time elapsed after turning on the air nozzle.

Author Manuscript Author Manuscript Author Manuscript Author Manuscript

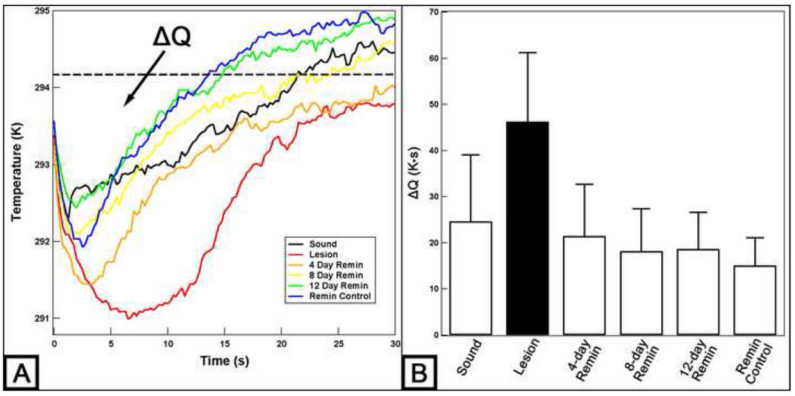


**Fig. 4.**

(A) Typical time-temperature profiles over 30 seconds of the sample shown in Fig. 2. ΔQ is the area enclosed by the dotted line representing the ambient temperature and the time-temperature curve. Mean ± S.D. (B) ΔQ measurements of the 24-hour demineralization samples. Bars not sharing any common colors were significantly different, $p < 0.05$ ($n = 15$).

Author Manuscript Author Manuscript Author Manuscript Author Manuscript

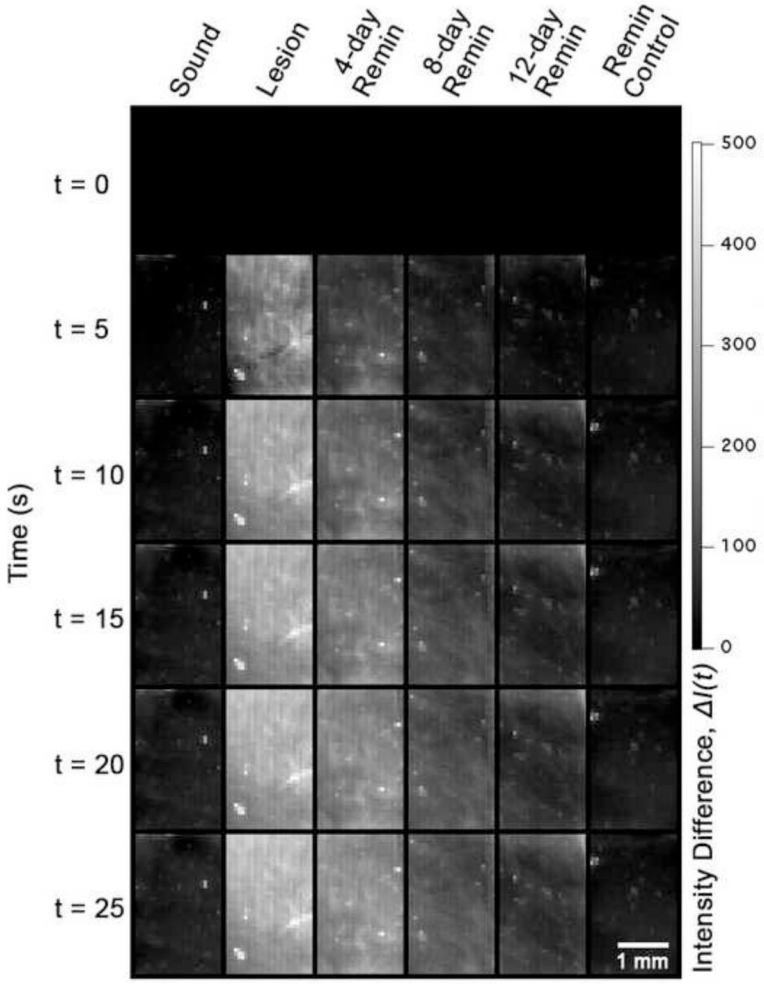


**Fig. 5.**

Time-lapse near-IR reflectance images with a 1460 nm band-pass filter of the sample shown in Fig. 2. Time axis on left represents time elapsed after turning on the air nozzle.

Author Manuscript Author Manuscript Author Manuscript Author Manuscript

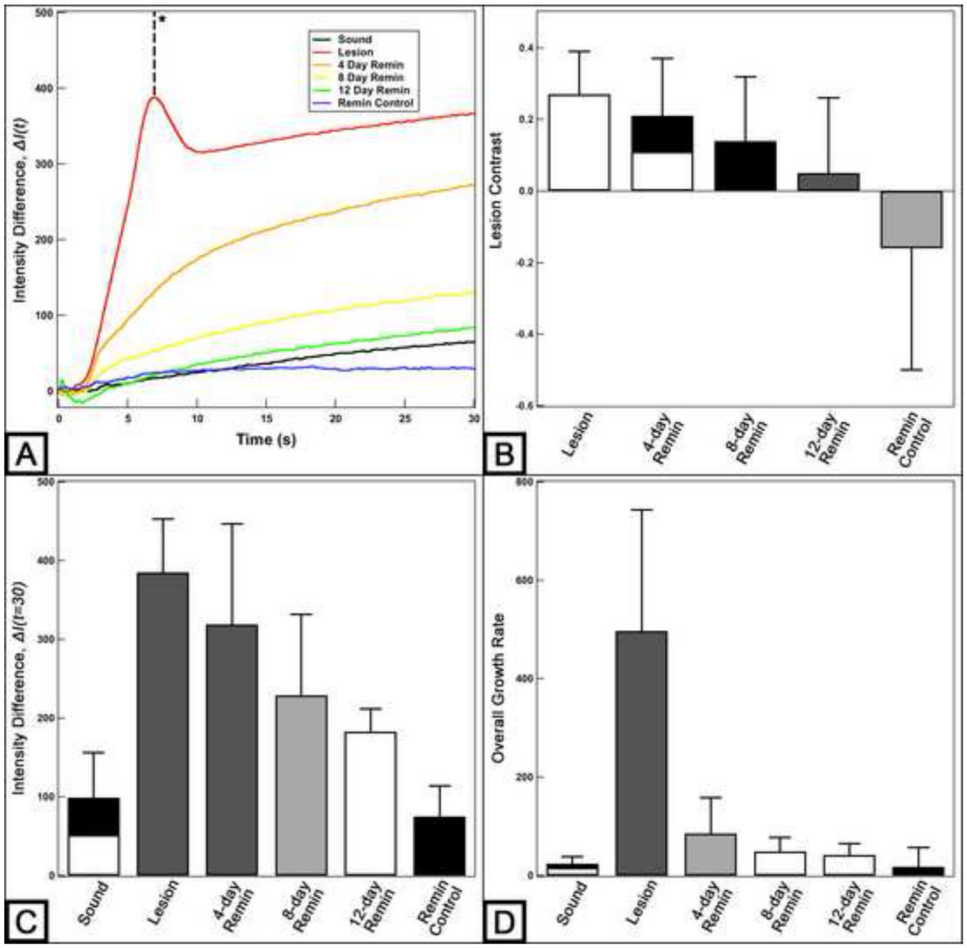


**Fig. 6.**

(A) Typical time-near-IR reflectance intensity difference profiles over 30 seconds of the sample shown in Fig. 2 when the 1460 nm band-pass filter was used. The time-intensity difference curve was cropped up to the dotted line* for curve fitting to the sigmoid function if the window exhibited a sudden excursion in intensity as shown in the lesion window (red). Mean ± S.D. (B) lesion contrast measurements, (C) intensity differences at t = 30 seconds and (D) OGR values acquired from the curve fitting of the 24-hour demineralization samples when the 1460 nm band-pass filter was used. Bars not sharing any common colors were significantly different, $p < 0.05$ (n = 15).

Author Manuscript Author Manuscript Author Manuscript Author Manuscript



**Table 1**

Mean ± S.D. of PS-OCT, PLM and TMR measurements for the 8 and 24 hr demineralization groups. Groups with the same letters are statistically similar, $P > 0.05$ in each row (n = 15).

| | Lesion | 4-day Remin | 8-day Remin | 12-day Remin | Remin Control |
|---|---|---|---|---|---|
| **24-hour Demineralization (n = 15)** | | | | | |
| Transparent Layer Thickness (PS-OCT, μm) | 0 a | 24.9 ± 5.3 b | 30.8 ± 4.7 c | 35.2 ± 6.1 d | 0 a |
| Transparent Layer Thickness (PLM, μm) | 0 a | 25.5 ± 6.6 b | 31.0 ± 4.6 c | 35.6 ± 4.6 d | 0 a |
| Lesion Body Depth (PS-OCT, μm) | 40.2 ± 6.1 a | 46.2 ± 10.6 a | 45.4 ± 11.6 a | 42.3 ±12.9 a | 0 b |
| Lesion Body Depth (PLM, μm) | 42.3 ± 8.1 a | 44.9 ± 9.5 a | 46.6 ± 10.0 a | 44.0 ± 15.9 a | 0 b |
| Integrated Reflectivity, ΔR (dB x μm) | 1033 ± 121 a | 952 ± 171 a,b | 900 ± 145 b | 777 ± 102 c | 0 d |
| Integrated Mineral Loss, ΔZ (vol % x μm) | 1433 ± 612 a | 736 ± 270 b | 693 ± 283 b | 393 ± 278 c | −43 ± 130 d |
| **8-hour Demineralization (n = 15)** | | | | | |
| Transparent Layer Thickness (PS-OCT, μm) | 1.3 ± 5.2 a* | 23.6 ± 5.6 b | 24.6 ± 5.5 b | 24.3 ± 7.7 b | 0 a |
| Transparent Layer Thickness (PLM, μm) | 1.2 ± 4.5 a* | 21.7 ± 5.0 b | 22.7 ± 6.3 b | 22.7 ± 8.2 b | 0 a |
| Lesion Body Depth (PS-OCT, μm) | 30.7 ± 7.6 a | 42.9 ± 9.2 b | 44.9 ± 15.9 b | 47.0 ± 14.3 b | 0 c |
| Lesion Body Depth (PLM, μm) | 29.3 ± 6.3 a | 29.8 ± 12.4 a | 26.4 ± 15 a | 20.0 ± 13.9 a | 0 b |
| Integrated Reflectivity, ΔR (dB x μm) | 790 ± 146 a | 734 ± 173 a | 756 ± 161 a | 666 ± 101 a | 0 b |
| Integrated Mineral Loss, ΔZ (vol % x μm) | 800 ± 317 a | 347 ± 264 b | 300 ± 257 b | 195 ± 262 b | 1 ± 129 c |

*One lesion window exhibited a transparent surface layer.

*J Dent*. Author manuscript; available in PMC 2016 August 01.

Author Manuscript Author Manuscript Author Manuscript Author Manuscript



**Table 2**

Mean ± S.D. for ΔQ from thermal imaging measurements for each window for the 8 and 24 hr demineralization groups. Groups with the same letters are statistically similar, P > 0.05 in each row (n = 15).

| | Sound | Lesion | 4 Day Remin | 8 Day Remin | 12 Day Remin | Remin Control |
|---|---|---|---|---|---|---|
| **24 Hour Demineralization (n = 15)** | | | | | | |
| ΔQ (K sec) | 24.7 ± 14.4 a | 46.3 ± 14.9 b | 21.5 ± 11.2 a | 18.2 ± 9.2 a | 18.7 ± 7.9 a | 15.1 ± 6.0 a |
| **8 Hour Demineralization (n = 15)** | | | | | | |
| ΔQ (K sec) | 15.6 ± 14.8 a | 24.6 ± 14.4 b | 9.6 ± 9.5 a | 7.9 ± 6.8 a | 9.0 ± 6.4 a | 8.8 ± 7.6 a |

*J Dent*. Author manuscript; available in PMC 2016 August 01.

Author Manuscript Author Manuscript Author Manuscript Author Manuscript





*J Dent*. Author manuscript; available in PMC 2016 August 01.

**Table 3**

Near-IR reflectance measurements: mean ± S.D. for lesion contrast measurements, intensity differences at t = 30 seconds ($\Delta I_{t=30}$) and overall growth rate (OGR) acquired from curve fitting for different spectral bands and periods of demineralization. Groups with the same letters are statistically similar, P > 0.05 in each row (n = 15).

| | Sound | Lesion | 4 Day Remin | 8 Day Remin | 12 Day Remin | Remin Control |
|---|---|---|---|---|---|---|
| **Wavelength λ= 1260–1340 nm, 24 Hour Demineralization (n = 15)** | | | | | | |
| Contrast | - | 0.14 ± 0.05 a | 0.15 ± 0.07 a | 0.13 ±0.09 a | 0.07 ± 0.11 b | −0.05 ± 0.15 c |
| ΔI(t = 30) | 60 ± 49 a | 201 ± 56 b | 176 ± 65 b | 113 ± 66 a,c | 98 ± 64 a,c | 38 ± 35 a,d |
| OGR | 19 ± 10 a,b,c | 311 ± 184 d | 46 ± 30 a | 28 ± 16 b | 24 ± 13 b | 13 ± 6 c |
| **λ= 1420–1500 nm** | | | | | | |
| Contrast | - | 0.27 ± 0.12 a | 0.21 ± 0.16 a,b | 0.14 ± 0.18 b | 0.05 ± 0.21 c | −0.16 ± 0.34 d |
| ΔI(t = 30) | 99 ± 57 a,b | 385 ± 68 c | 319 ± 128 c | 229 ± 103 d | 183 ± 79 a | 75 ± 39 b |
| OGR | 24 ± 14 a,b | 497 ± 246 c | 85 ± 73 a | 49 ± 28 a | 42 ± 23 a | 18 ± 10 b |
| **λ= 1400–1700 nm** | | | | | | |
| Contrast | - | 0.19 ± 0.11 a | 0.18 ± 0.13 a | 0.15 ± 0.15 a | 0.05 ± 0.16 b | −0.16 ± 0.31 c |
| ΔI(t = 30) | 166 ± 81 a,b | 679 ± 147 c | 555 ± 240 c | 386 ± 224 a | 310 ± 163 a | 129 ± 79 b |
| OGR | 45 ± 20 a,b | 898 ± 422 c | 134 ± 70 d | 92 ± 50 a | 76 ± 41 a | 32 ± 18 b |
| **λ= 1500–1700 nm** | | | | | | |
| Contrast | - | 0.21 ± 0.06 a | 0.21 ± 0.93 a,b | 0.17 ± 0.12 b | 0.09 ± 0.11 c | −0.08 ± 0.22 d |
| ΔI(t = 30) | 103 ± 51 a,b | 325 ± 86 c | 295 ± 127 c | 200 ± 111 a | 163 ± 86 a | 67 ± 50 b |
| OGR | 23 ± 12 a,b,c | 441 ± 219 d | 78 ± 66 a | 43 ± 26 b | 39 ± 20 b | 15 ± 10 c |
| **Wavelength λ= 1260–1340 nm, 8 Hour Demineralization (n = 15)** | | | | | | |
| Contrast | - | 0.13 ± 0.08 a b c | 0.15 ± 0.13 a,b | 0.14 ± 0.17 a | 0.09 ± 0.20 b | −0.02 ± 0.27 c |
| ΔI(t = 30) | 38 ± 59 a | 128 ± 78 b | 88 ± 69 a | 67 ± 72 a | 73 ± 60 a,b | 47 ± 38 a |
| OGR | 9 ± 25 a | 36 ± 19 b | 19 ± 15 a | 15 ± 12 a | 23 ± 22 a,b | 16 ± 14 a |
| **λ= 1420–1500 nm** | | | | | | |
| Contrast | - | 0.18 ± 0.15 a,b | 0.16 ± 0.17 a,b | 0.13 ± 0.26 a | 0.05 ± 0.31 b | −0.09 ± 0.33 c |
| ΔI(t = 30) | 69 ± 67 a | 225 ± 81 b | 127 ± 74 c | 112 ± 73 a,c | 124 ± 71 c | 82 ± 37 a,c |
| OGR | 15 ± 8 a | 83 ± 40 b | 23 ± 14 a | 18 ± 13 a | 26 ± 26 a | 17 ± 7 a |
| **λ= 1400–1700 nm** | | | | | | |
| Contrast | - | 0.22 ± 0.11 a,b | 0.20 ± 0.14 a,b | 0.20 ± 0.17 a | 0.10 ± 0.22 b | −0.05 ± 0.29 c |

Author Manuscript Author Manuscript Author Manuscript Author Manuscript



| | Sound | Lesion | 4 Day Remin | 8 Day Remin | 12 Day Remin | Remin Control |
|---|---|---|---|---|---|---|
| ΔI(t = 30) | 140 ± 98 a | 436 ± 224 b | 259 ± 173 c | 203 ± 157 a | 201 ± 119 a | 156 ± 91 a |
| OGR | 32 ± 19 a,b | 166 ± 116 b | 47 ± 31 a | 32 ± 25 b | 44 ± 36 a,b | 31 ± 15 a,b |
| **λ= 1500–1700 nm** | | | | | | |
| Contrast | - | 0.20 ± 0.12 a,b | 0.17 ± 0.18 a,b | 0.15 ± 0.25 a | 0.08 ± 0.26 b | −0.03 ± 0.30 c |
| ΔI(t = 30) | 68 ± 52 a | 212 ± 101 b | 139 ± 82 c | 106 ± 76 a,c | 109 ± 58 a,c | 80 ± 39 a,c |
| OGR | 15 ± 11 a | 58 ± 24 b | 25 ± 16 c | 17 ± 13 a,c | 19 ± 11 a,c | 13 ± 7 a,c |

*J Dent*. Author manuscript; available in PMC 2016 August 01.